

A novel image space formalism of Fourier domain interpolation neural networks for noise propagation analysis

P. Dawood^{1,3*}, F. Breuer², I. Homolya⁴, J. Stebani^{1,2}, M. Gram^{1,5}, P.M. Jakob¹, M. Zaiss³ and M. Blaimer²

¹ Experimental Physics 5, University of Würzburg, Würzburg, Germany

² Magnetic Resonance and X-ray Imaging Department, Fraunhofer Institute for Integrated Circuits IIS, Division Development Center X-Ray Technology, Würzburg, Germany

³ Institute of Neuroradiology, University Hospital Erlangen, Erlangen, Germany

⁴ Molecular and Cellular Imaging, Comprehensive Heart Failure Center, University Hospital Würzburg, Würzburg, Germany

⁵ Department of Internal Medicine I, University Hospital Würzburg, Würzburg, Germany

*Correspondence to: Peter Dawood

Department of Physics, University of Würzburg

Experimental Physics 5

Am Hubland, 97074 Würzburg, Germany

Email: peter.dawood@uni-wuerzburg.de

Word Counts (Abstract): 248

Word Counts (Body): Approx. 3180

Number of Figures and Tables: 5

Number of Citations: 29

Submitted as Technical Note for Peer-Review to Magnetic Resonance in Medicine

Abstract

Purpose To develop an image space formalism of multi-layer convolutional neural networks (CNNs) for Fourier domain interpolation in MRI reconstructions and analytically estimate noise propagation during CNN inference.

Theory and Methods Nonlinear activations in the Fourier domain (also known as k-space) using complex-valued Rectifier Linear Units are expressed as elementwise multiplication with activation masks. This operation is transformed into a convolution in the image space. After network training in k-space, this approach provides an algebraic expression for the derivative of the reconstructed image with respect to the aliased coil images, which serve as the input tensors to the network in the image space. This allows the variance in the network inference to be estimated analytically and to be used to describe noise characteristics. Monte-Carlo simulations and numerical approaches based on auto-differentiation were used for validation. The framework was tested on retrospectively undersampled in vivo brain images.

Results Inferences conducted in the image domain are quasi-identical to inferences in the k-space, underlined by corresponding quantitative metrics. Noise variance maps obtained from the analytical expression correspond with those obtained via Monte-Carlo simulations, as well as via an auto-differentiation approach. The noise resilience is well characterized, as in the case of classical Parallel Imaging. Komolgorov-Smirnov tests demonstrate Gaussian distributions of voxel magnitudes in variance maps obtained via Monte-Carlo simulations.

Conclusion The quasi-equivalent image space formalism for neural networks for k-space interpolation enables fast and accurate description of the noise characteristics during CNN inference, analogous to geometry-factor maps in traditional parallel imaging methods.

Keywords: RAKI, GRAPPA, Parallel Imaging, convolutional neural network, saliency map, g-factor, noise propagation

1. Introduction

The GeneRalized Autocalibrating Partial Parallel Acquisition (GRAPPA)(1) is a widely used classic parallel imaging method operating in k-space. It estimates missing signals by convolution of adjacent, multichannel signals. The convolution filters are calibrated by linear least-squares fitting using several fully sampled auto-calibration signals (ACS). However, such matrix systems are typically ill-conditioned at high accelerations resulting in severe noise amplification, which is a major limitation of PI.

To enhance noise resilience, GRAPPA has been generalized using a deep learning method called Robust Artificial Neural Networks for k-space Interpolation (RAKI)(2). RAKI employs multi-layer feature extraction and applies nonlinear activation functions to convolution layers, which are essential elements of convolutional neural networks (CNNs). RAKI represents the nonlinear extension of GRAPPA within a neural network architecture. RAKI's neural network parameters (i.e. CNN filters) are calibrated using scan-specific ACS as training data. It has demonstrated superior performance over GRAPPA by improving the signal-to-noise ratio (SNR)(2)(3).

However, achieving clinical translation of machine learning reconstruction methods requires consistency, transparency, and reproducibility. Understanding the noise propagation in neural networks is crucial for leveraging the black-box nature of such algorithms. Furthermore, the performance of neural network reconstructions is typically quantified using metrics such as normalized mean squared error (NMSE), peak SNR (PSNR) and structural similarity index measure (SSIM), which require a fully-sampled reference image. Thus, prospectively undersampled scans reconstructed with CNNs lack quality control, and a reference-free quality metric is desirable. In classical linear PI, the geometry factor (g-factor) quantifies noise amplification resulting from the reconstruction algorithm. Analytical expressions exist for both sensitivity encoding (SENSE)(4) and GRAPPA g-factors(5). The GRAPPA g-factor estimation requires the reconstruction process (also known as inference) to be formulated in the image space domain. However, a more generalized g-factor adaptation for k-space interpolation using CNNs has not been presented yet. Previous evaluations of noise propagation in deep learning image reconstructions, including RAKI, have primarily relied on Monte Carlo simulations(6) or auto-differentiation approaches(7), both of which can be time consuming.

Here, we present a novel, generalized analytical g-factor expression for k-space interpolation reconstructions based on multi-layer CNNs. To this end, an image space formalism is proposed considering the effect of multiple convolution layers as well as nonlinear activation functions on the noise characteristics.

The main contributions of this study include the introduction of an image space formalism of RAKI for quasi-identical inference in image space and the formulation of a generalized g-factor for network noise propagation analysis. Furthermore, we analyze the noise distribution in the reconstructed images.

2. Theory

Before introducing the image space formalism, the conventional RAKI signal processing in k-space is briefly reviewed. Translation of convolution weights and activation functions from k-space to image domain is then introduced. A novel analytic description of RAKI g-factor is then obtained via the algebraic derivatives of the image reconstruction w.r.t. the aliased coil images.

Review of RAKI

A review of RAKI can be found in(2)(8). Let $S_0 \in \mathbb{C}^{N_x \times N_y \times N_c}$ denote the zero-filled, undersampled k-space with $N_{x,y}$ denoting the image dimensions, and N_c the total coil number. S_0 is processed sequentially through hidden layers for abstract feature extraction. The signal of the n th hidden layer $S_n \in \mathbb{C}^{N_x \times N_y \times N_c^n}$ is obtained via a subsequent convolution and nonlinear activation operation

$$S_n = \mathbb{C}\text{LReLU}(S_{n-1} \circledast w_n), \quad n = 1, \dots, N^{hid} \quad (1)$$

where \circledast denotes a complex-valued convolution, N^{hid} is the total number of hidden layers and $w_n \in \mathbb{C}^{k_x^n \times k_y^n \times N_c^{n-1} \times N_c^n}$ is the convolution kernel of the n th hidden layer with $[k_x^n, k_y^n]$ denoting the kernel size (i.e. convolution filter size) assigned to the n th hidden layer, and $[N_c^{n-1}, N_c^n]$ denoting the channel numbers assigned to the $(n-1)$ th and n th hidden layers, respectively. The complex, leaky Rectifier Linear Unit ($\mathbb{C}\text{LReLU}$)(9)(10) introduces the nonlinearity and applies the LReLU separately to the real- and imaginary part of the signal to be activated S'_n :

$$S_n = \mathbb{C}\text{LReLU}(S'_n) = \text{LReLU}(\text{Re}\{S'_n\}) + i\text{LReLU}(\text{Im}\{S'_n\}) \quad (2)$$

where

$$\text{LReLU}(q) = \begin{cases} q & q > 0 \\ a*q & \text{otherwise} \end{cases} \quad (3)$$

is applied elementwise to $\text{Re}\{S'_n\}$ and $\text{Im}\{S'_n\}$ independently. The slope-parameter a is a pre-defined hyperparameter. The final layer is activated with the identity operator $\text{id}(x) = x$

$$S_{int} = \text{id}(S_{N^{hid}} \circledast w_{int}) = S_{N^{hid}} \circledast w_{int} \quad (4)$$

where $S_{N^{hid}}$ is the signal of the final hidden layer, $w_{int} \in \mathbb{C}^{k_x^{int} \times k_y^{int} \times N_c^{N^{hid}} \times R}$ is the convolution kernel of the final layer and $S_{int} \in \mathbb{C}^{N_x \times N_y \times R}$ are the interpolated k-space signals, where R denotes the undersampling rate.

During training, the convolution kernels $w_{1,\dots,N^{hid}}$ and w_{int} are calibrated using ACS by minimizing the L_2 error of interpolated and ground truth signals. RAKI is described as a scan-specific reconstruction as the CNN filters are trained for each scan separately.

2.1. Image space formalism of RAKI

An integral part of the concept presented in this work is to transfer the individual building blocks of RAKI (Eq. 1) into an image space formalism. According to the convolution theorem, the action of the convolution to the k-space signal S_{n-1} in Eq.1 is an elementwise multiplication in the image space. This has previously been demonstrated for GRAPPA reconstructions(5)(11). However, transferring the action of the nonlinear activation requires dedicated considerations: Let S'_n denote the signal in the n th hidden layer prior to activation. As can be seen from Eqs.2 and 3, the application of $\mathbb{C}\text{LReLU}$ leaves S'_n values greater than zero unchanged, otherwise, scales with the slope parameter a . Thus, the application of $\mathbb{C}\text{LReLU}$ in k-space can be viewed equivalently as an elementwise multiplication of S'_n with an introduced *activation mask* $A \in \mathbb{C}^{N_x \times N_y \times N_c^n}$ (Fig.1A):

$$S_n = \mathbb{C}\text{LReLU}(S'_n) = S'_n \odot A \quad (5)$$

where \odot denotes a complex-valued, elementwise multiplication. First, *binary masks* $M_{\text{Re,Im}}$ are defined for the real and imaginary parts of S'_n according to:

$$M_{\text{Re,Im}} = \begin{cases} 1 & \text{if } \text{Re}\{S'_n\}, \text{Im}\{S'_n\} > 0 \\ a & \text{if } \text{Re}\{S'_n\}, \text{Im}\{S'_n\} \leq 0. \end{cases} \quad (6)$$

The activation masks A are then obtained by

$$\begin{aligned} S'_n \odot A &= (M_{\text{Re}} \cdot \text{Re}\{S'_n\} + i M_{\text{Im}} \cdot \text{Im}\{S'_n\}) \\ \Leftrightarrow A &= (M_{\text{Re}} \cdot \text{Re}\{S'_n\} + i M_{\text{Im}} \cdot \text{Im}\{S'_n\}) \cdot \frac{S'_n{}^*}{|S'_n|^2}, \end{aligned} \quad (7)$$

where $S'_n{}^*$ is the complex-conjugate of S'_n . By formulating the action of $\mathbb{C}\text{LReLU}$ to signal S'_n as described in Eq. 5, the elementwise multiplication of S'_n with A in k-space can be translated into a corresponding convolution operation in image space, according to the convolution theorem. Thus, the elementary building block of RAKI in k-space translates into the image domain according to:

$$\mathbb{C}\text{LReLU}(S_{n-1} \otimes w_n) = (S_{n-1} \otimes w_n) \odot A_n \xrightarrow{(I)\text{FFT}} (\widehat{S}_{n-1} \odot \widehat{w}_n) \otimes \widehat{A}_n, \quad (8)$$

where \widehat{S}_{n-1} , \widehat{w}_n and \widehat{A}_n are the inverse Fourier transformations of S_{n-1} , w_n and A_n , respectively.

Eq.8 allows the formulation of RAKI reconstruction (i.e. inference) entirely in image space (Fig.1C):

$$\begin{aligned} \widehat{S}_n &= (\widehat{S}_{n-1} \odot \widehat{w}_n) \otimes \widehat{A}_n, \quad (9) \\ \text{and } \widehat{S}_{int} &= \widehat{S}_{N^{hid}} \odot \widehat{w}_{int} \end{aligned}$$

where $\widehat{w}_{1,\dots,N^{hid}}$, $\widehat{A}_{1,\dots,N^{hid}}$ and $\widehat{w}_{int} \in \mathbb{C}^{N_x \times N_y \times N_c^{hid} \times N_c}$ are the image space reconstruction parameters. When the convolution kernels as well as the activation masks are trained in k-space and transferred into the image space, RAKI inference can be performed entirely in the image space following Eq.9. In the following, the spatial dimensions are merged $N = N_x \times N_y$ for readability.

The unfolded coil images $\widehat{S}_{int} \in \mathbb{C}^{N \times N_c}$ are finally combined to the reconstructed image $\widehat{S}_{acc} \in \mathbb{C}^N$ using coil-combination weights $\mathbf{p} \in \mathbb{C}^{N \times N_c}$: $\widehat{S}_{acc} = \mathbf{p} \cdot \widehat{S}_{int}^T$.

2.2. Generalized g-factor formulation

The g-factor is defined for each voxel as the SNR in the fully-sampled reference image SNR_{full} , divided by the SNR in the reconstructed, coil-combined image SNR_{acc} (4)(5):

$$\mathbf{g} = \frac{SNR_{full}}{SNR_{acc} \sqrt{R}} = \frac{\sqrt{\text{Var}_{acc}}}{\sqrt{\text{Var}_{full}} \sqrt{R}} \quad (10)$$

where R denotes the undersampling rate. The variance of the coil combined image Var_{acc} can be estimated using the Jacobians of \widehat{S}_{acc} w.r.t. the aliased coil images \widehat{S}_0 . Let $\mathbf{J}^{int} = \partial \widehat{S}_{int} / \partial \widehat{S}_0 \in \mathbb{C}^{N \times N_c \times N \times N_c}$ denote the Jacobian of the unfolded coil images w.r.t. the aliased coil images, then the chain rule leads to $\mathbf{J}^{acc} = \partial \widehat{S}_{acc} / \partial \widehat{S}_0 \in \mathbb{C}^{N \times N \times N_c} = \mathbf{p} \cdot \mathbf{J}^{int}$. The variance of \widehat{S}_{acc} is obtained in first order approximation by $\text{Var}_{acc} = (\mathbf{p} \cdot \mathbf{J}^{int}) \Sigma^2 (\mathbf{p} \cdot \mathbf{J}^{int})^T$, with Σ denoting the coil-array noise covariance matrix. Thus, for the g-factor, we obtain:

$$\mathbf{g} = \frac{\sqrt{\text{Var}_{acc}}}{\sqrt{\text{Var}_{full}} \sqrt{R}} = \sqrt{\frac{(\mathbf{p} \cdot \mathbf{J}^{int}) \Sigma^2 (\mathbf{p} \cdot \mathbf{J}^{int})^T}{\mathbf{p} \Sigma^2 \mathbf{p}^T}} \frac{\mathbf{1}}{\sqrt{R}} \quad (11)$$

The following section describes how to obtain \mathbf{J}^{int} from the RAKI image space inference presented in section 2.2.

2.3. Algebraic expression of Jacobians in the convolutional neural network

The image space formulation of RAKI (Eq.9) provides an algebraic expression of the derivative of the output tensor of each hidden layer w.r.t. the input tensor of that layer. Note that the convolution with the activation mask A can be viewed as matrix multiplication using a Toeplitz matrix representation of A . Eq.9 can then be expressed as

$$\widehat{\mathbf{S}}_n(\mathbf{l}, \mathbf{h}) = \sum_{r=1}^N \sum_{k=1}^{N_c^{n-1}} \widehat{\mathbf{S}}_{n-1}(\mathbf{r}, \mathbf{k}) \cdot \widehat{\mathbf{w}}_n(\mathbf{r}, \mathbf{h}, \mathbf{k}) \cdot \widehat{\mathbf{A}}_n(\mathbf{l}, \mathbf{r}, \mathbf{h}), \quad n = 1, \dots, N^{hid} \quad (12)$$

$$\text{and } \widehat{\mathbf{S}}_{int}(\mathbf{l}, \mathbf{h}) = \sum_{k=1}^{N_c^{N^{hid}}} \widehat{\mathbf{S}}_{N^{hid}}(\mathbf{l}, \mathbf{k}) \cdot \widehat{\mathbf{w}}_{int}(\mathbf{l}, \mathbf{h}, \mathbf{k})$$

The Jacobian $J^n = \partial \widehat{\mathbf{S}}_n / \partial \widehat{\mathbf{S}}_{n-1} \in \mathbb{C}^{N \times N_c^n \times N \times N_c^{n-1}}$ follows from Eq.12, and its elements are:

$$J_{l,c;m,n}^n = \frac{\partial \widehat{\mathbf{S}}_n(\mathbf{l}, \mathbf{c})}{\partial \widehat{\mathbf{S}}_{n-1}(\mathbf{m}, \mathbf{n})} = \widehat{\mathbf{w}}_n(\mathbf{m}, \mathbf{c}, \mathbf{n}) \cdot \widehat{\mathbf{A}}_n(\mathbf{l}, \mathbf{m}, \mathbf{c}), \quad (13)$$

To obtain the derivative of each voxel in the unfolded coil images $\widehat{\mathbf{S}}_{int}$ w.r.t each voxel in the aliased coil images $\widehat{\mathbf{S}}_0$, i.e. $J^{int} = \partial \widehat{\mathbf{S}}_{int} / \partial \widehat{\mathbf{S}}_0 \in \mathbb{C}^{N \times N_c \times N \times N_c}$, the chain rule leads recursively to:

$$J_{l,h;m,n}^{int} = \frac{\partial \widehat{\mathbf{S}}_{int}(\mathbf{l}, \mathbf{h})}{\partial \widehat{\mathbf{S}}_0(\mathbf{m}, \mathbf{n})} = \sum_{k=1}^{N_c^{N^{hid}}} \widehat{\mathbf{w}}_{int}(\mathbf{l}, \mathbf{h}, \mathbf{k}) \cdot \sum_{z,t} J_{l,k;z,t}^{N^{hid}} \cdot \sum_{e,d} J_{z,t;e,d}^{N^{hid}-1} \cdot (\dots) \cdot \sum_{u,i} J_{e,d;u,i}^2 \cdot J_{u,i;m,n}^1 \quad (14)$$

These Jacobians are needed to obtain the RAKI g-factor by inserting Eq.14 into Eq.11.

The GRAPPA reconstruction in image space reduces to $\widehat{\mathbf{w}}_{int}$ only in Eq.9. Thus, J^{int} simplifies in Eq. 14 to:

$$\widehat{\mathbf{S}}_{int}(\mathbf{l}, \mathbf{h}) = \sum_{k=1}^{N_c} \widehat{\mathbf{S}}_0(\mathbf{l}, \mathbf{k}) \cdot \widehat{\mathbf{w}}_{int}(\mathbf{l}, \mathbf{h}, \mathbf{k}) \Rightarrow J^{int} = \frac{\partial \widehat{\mathbf{S}}_{int}}{\partial \widehat{\mathbf{S}}_0} = \widehat{\mathbf{w}}_{int} \quad (15)$$

When $J^{int} = \widehat{\mathbf{w}}_{int}$, we obtain the GRAPPA g-factor in Eq. 11.

3. Methods

The image space formalism for RAKI inferences, and noise propagation analysis was tested on two transversal 2D brain datasets. They were acquired from healthy volunteers at 3T (Siemens Magnetom Skyra, Siemens Healthineers, Erlangen, Germany) using a 20-channel head-neck coil array. All experimental procedures were in accordance with institutional guidelines and the study complied with the Helsinki Declaration on Human Experimentation. A T1w FLASH was acquired using TR/TE=250/2.9ms, flipangle=70°, FOV=230×230mm², matrix-size=320×320, slice thickness=3.0mm, activated coils=16. A T2w TSE was acquired using turbofactor=12, TR/TE=6000.0/100.0ms, FOV=256×256mm², matrix size=264×256, slice thickness=2.0mm, activated coils=20.

3.1. Domain quasi-equivalence and influence of nonlinear activation

Experiments showing the quasi-equivalence of RAKI inference in both domains, as well as g-factor evaluations were performed on 4-6 fold retrospectively undersampled datasets. The importance of nonlinear activation functions for RAKI noise resilience was demonstrated by performing RAKI training both with and without **CLReLU** activations. The network architecture used in this work included 2 hidden layers with 128- and 64 channels, respectively. ADAM(12) was used as optimizer.

Evaluations were performed both qualitatively using difference maps to references and quantitatively using NMSE, SSIM(13) and PSNR. We masked all reconstructions to outline the brain structures while

excluding non-brain areas (masks obtained via ESPIRiT(14)). ACS data were not reinserted. All reconstructions were performed offline using the Python language (v3.11.5) within the PyTorch deep learning framework(15) (v2.1.1) and were conducted on a high-performance-computing cluster with Intel XeonGold 6134(CPU, 360GB RAM).

3.2. Monte-Carlo simulations and automatic differentiation

Analytic g-factor maps were compared with maps obtained through Monte-Carlo simulations (also known as pseudo-multiple replica approach(16)). The reconstruction was repeated 1,000 times in image space using k-space data superimposed with randomly generated Gaussian noise $N(\mu = 0, \sigma^2 = 1)$. k-Space data was pre-whitened beforehand. The variance maps were estimated voxel-wise across the image stack, and g-factor maps were obtained according to Eq.10.

Automatic differentiation, also known as auto-differentiation, is a widely used technique in machine learning. It enables efficient computation of derivatives in complex mathematical expressions(17). Eqs.12 and 13 provide an algebraic expression for the derivative of voxels in the coilcombined reconstructed image w.r.t. voxels in the aliased coil images J^{acc} . Alternatively, J^{acc} can also be obtained using auto-differentiation frameworks.

We compared the analytic g-factor maps obtained via algebraic expressions with those obtained via auto-differentiation. The gradients $J_j^{acc} \in \mathbb{C}^{N \times N_c}$ of all voxels j in the coil-combined reconstructed image w.r.t the aliased coil images were calculated subsequently(7), and the corresponding g-factors according to Eq.11.

3.3. Noise distribution analysis in Monte-Carlo simulations

Via activation, RAKI introduces nonlinearities into the reconstruction pipeline, which may lead to non-Gaussian noise propagations. Thus, the validity of Eq. 11 needs to be evaluated. To determine if the distribution of voxel-magnitudes in the pseudo-replicas conforms to a normal distribution, the Kolmogorov-Smirnov (KS) normality test was applied with a sample size of 10,000. The KS test evaluates whether a given sample adheres to a normal distribution, which is considered as the null hypothesis(18). A p-value is calculated by comparing the test statistic to a distribution of the KS test statistic under the null hypothesis (significance level 0.05).

3.4. SNR dependence

Analytical g-factor maps were computed for different base line SNR levels. The pre-whitened raw data was superimposed with Gaussian noise with elevated standard deviations ($\sigma = 3$ and $\sigma = 5$). Noise was added both to the retrospectively undersampled data and to the fully sampled reference data. The g-factor maps were compared to those obtained via Monte-Carlo simulations.

4. Results

4.1. Domain quasi-equivalence and influence of nonlinear activation

Fig.2 depicts k-space reconstructions for the 4- and 5-fold retrospectively undersampled FLASH dataset. The noise resilience in RAKI is clearly displayed in the corresponding error maps and supported by significantly reduced NMSE and improved SSIM and PSNR values compared to GRAPPA. As proposed in this work, the RAKI inference was performed in the image domain. Quasi-identical error maps and quantitative metrics verify quasi-equivalence to the k-space reconstructions. Minor deviations may be attributed to convolution weights padding, as they also appear in GRAPPA image-domain inferences.

It is worth noting that the noise suppression in RAKI can be attributed to nonlinear activations. When the nonlinear activation was replaced by the identity operator (i.e. a linear activation), RAKI converges towards GRAPPA (Fig.2), demonstrated both qualitatively and quantitatively. Similar results for the TSE dataset at 5- and 6-fold retrospective undersampling are shown in Fig.S1.

4.2. Monte-Carlo, auto-differentiation and analytical g-factor maps

Fig. 3A shows the 50x50 low-resolution g-factor maps of the reconstructions presented in Fig.2. The maps obtained through the proposed analytical expression match those obtained through Monte-Carlo simulations accurately for all experiments for both RAKI and GRAPPA (Fig.3B). The spatially resolved noise resilience is well-characterized in RAKI in comparison to GRAPPA, and in agreement with error maps in Fig.2. The g-factor maps of the TSE dataset (Fig.S1) are included in Fig.S2.

The RAKI g-factor maps obtained with auto-differentiation are identical to those obtained analytically. This is expected since both methods compute the same Jacobians. However, there is a significant difference in computation time. The analytical g-factor maps were calculated within 166.5–174.2 seconds in all imaging scenarios for RAKI (0.2–0.3 seconds for GRAPPA), while the auto-differentiation technique required 5,125.1–5,625.0 seconds (470.7–479.9 seconds for GRAPPA), resulting in a time cost of ≈ 2.2 seconds per voxel (≈ 0.2 seconds/voxel for GRAPPA). The Monte-Carlo simulations required 857.3–913.1 seconds (6.3–48.9 for GRAPPA) for a total of 1,000 pseudo replicas, resulting in a time cost of ≈ 0.9 seconds per repetition for RAKI.

4.3. Noise distribution analysis in Monte-Carlo simulations

The normal distribution of voxel magnitudes was validated in Monte-Carlo simulations. Fig.4A shows the standard deviation maps for the 5-fold undersampled FLASH dataset. The KS test was performed by fitting of the voxel magnitudes to a normal function. In Fig. 4B, this is shown for 4 representative voxels located at dedicated points (A-D) in the standard deviation map. At B, pulsatile bloodflow artifacts cause an elevated standard deviation, while at A and C, they are elevated due to the multiple folding of pixels, resulting from the undersampling rate and geometric imaging settings. At D, the standard deviation decreases as the voxels can be unfolded with high accuracy. However, the histograms of all voxel indicate normal distributions. The p-value maps are shown in the top rows of Fig. 4C. In the bottom rows of Fig. 4C, a binary mask indicates voxels that exhibit p-values greater than 0.05. A normal distribution can be assumed for almost all voxels (TSE dataset at 6-fold retrospective undersampling shown in Fig.S3).

4.4. SNR dependence

Fig. 5 shows RAKI g-factor maps of the FLASH dataset (4-fold undersampled) which was superimposed with Gaussian noise with increasing standard deviations. The enforced SNR loss is visible in the image reconstructions and error maps (Fig. 5A), as well as in the quantitative SNR maps obtained from Monte-Carlo simulations (Fig. 5D). For those cases, the analytical g-factor maps are still in good agreement with those maps obtained via the Monte-Carlo simulations (Fig.5 B and C). Similar results can be observed for the TSE dataset (5-fold retrospective undersampled) and are shown in Fig. S4. The results also confirm the so-called GRAPPA paradox and show that higher noise in the ACS has a similar effect like Tikhonov regularization thereby yielding lower g-factors(19).

5. Discussion

The noise propagation in CNNs for k-space interpolation has been investigated analytically, via Monte-Carlo simulations and via auto-differentiation. A novel image space formalism for network inference has been presented, which enables a fast and analytical description of the noise characteristics.

Kolmogorov-Smirnov tests show that Gaussian noise distribution is maintained after RAKI reconstruction, even though nonlinear activation functions are applied.

It has also been demonstrated that noise resilience in RAKI can be attributed to nonlinear activations of the hidden layers. RAKI with linear activation function basically represents an extended GRAPPA with multiple hidden layers, but does not yield significant reconstruction performance.

The activation in k-space is formulated as a complex, elementwise multiplication of the signal with an introduced activation mask. This translates the activation into a convolution in the image space. It is this convolution in image space that leads to the noise resilience in RAKI. However, as the convolution operation introduces correlation between voxels, this operation can be viewed as an image filter and may come along with potential blurring. The framework presented here allows to study the potential impact of the activation function in more detail within each layer and within each channel.

The RAKI g-factor may be used as an analytical, fast reconstruction measure when no references are available. Furthermore, NMSE and SSIM are not specific to noise artifacts, but influenced by other reconstruction errors such as residual aliasing or pulsatile bloodflow. The analytical quantification of noise characteristics may be combined with quantifications of induced blurring, that potentially comes along with the noise suppression, as it relies on a convolution in image space. This could lead to a new set of quantitative, exact metrics, dedicated to scan-specific image reconstructions with CNNs. Thus, the description of the network inference in the image space opens new paths to gain insights into the functionality of k-space interpolation networks. This may also lead to further optimizations regarding cost functions or network architectures. In a broader context, such metric maps are analogous to so called saliency maps known from deep learning. They highlight the most influential regions in an input data point for a model's output(20)(21). Saliency maps serve as crucial interpretability tools, aiding in the comprehension and interpretability of complex deep learning models across various applications, including healthcare(22)(23). In the context of image reconstruction, saliency maps have also been used for uncertainty quantification (24)(25)(26)(27).

Compared to Monte-Carlo and auto-differentiation, the analytical approach is the fastest and most accurate. While auto-differentiation is equally accurate, it demands significantly more computation time. However, its advantage lies in its relatively simple implementation. Monte-Carlo simulations share this attribute but may also require increased computation time depending on replica number and desired accuracy.

Calculating the Jacobian of the coil-combined, reconstructed image relative to the aliased coil images requires computing intermediate Jacobians on hidden layers. If one layer has 64 channels and the next has 128, the intermediate Jacobian is of size $[N,128,N,64]$ and consumes 250-300Gb of memory for low-resolution images ($N=50 \times 50$). Therefore, memory demand is a limitation of this approach. Alternatively, one could compute Jacobians batch-wise, but this reduces time efficiency compared to Monte Carlo and auto-differentiation. Alternatively, reducing image resolution to 32×32 still adequately captures noise characteristics, with a g-factor map typically calculated within seconds.

This work was limited to 2D imaging but can be extended to CAIPIRINHA (28)(29). However, this demands higher memory costs, and dedicated parallel computation techniques are required.

6. Conclusion

Nonlinear activation of k-space signals within CNNs can be expressed as elementwise multiplication with an activation mask, which translates into a convolution in the image space. This enables formulation of a quasi-identical image space formalism for network inference. The Jacobians of the coil-combined reconstructed image w.r.t. the aliased coil images can be expressed algebraically. Thus, the noise variance can be calculated analytically in first order approximation. This enables fast and

accurate description of the noise characteristics, analogous to g-factor maps in traditional parallel imaging methods.

Acknowledgements

Funding Information

This research project received support from the Bavarian Ministry of Economic Affairs, Infrastructure, Transport and Technology.

Data availability statement

In the spirit of reproducible research, code of the RAKI image space formalism and g-factor computation is available under the following link: <https://github.com/pdawood/imageSpaceRaki>

References

- (1) Griswold MA, Jakob PM, Heidemann RM, Nittka M, Jellus V, Wang J, et al. Generalized autocalibrating partially parallel acquisitions (GRAPPA). *Magnetic Resonance in Medicine*. 2002;47(6):1202–1210.
- (2) Akçakaya M, Moeller S, Weingärtner S, Uğurbil K. Scan-specific robust artificial-neural-networks for k-space interpolation (RAKI) reconstruction: Database-free deep learning for fast imaging. *Magnetic Resonance in Medicine*. 2019;81(1):439–453.
- (3) Dawood P, Breuer F, Stebani J, Burd P, Homolya I, Oberberger J, Jakob PM, Blaimer M. Iterative training of robust k-space interpolation networks for improved image reconstruction with limited scan specific training samples. *Magnetic Resonance in Medicine*. 2023;89(2):812.827.
- (4) Pruessmann KP, Weiger M, Scheidegger MB, Boesiger P. SENSE: Sensitivity encoding for fast MRI. *Magnetic Resonance in Medicine*. 1999;42(5):952–962.
- (5) Breuer FA, Kannengiesser SAR, Blaimer M, Seiberlich N, Jakob PM, Griswold MA. General formulation for quantitative G-factor calculation in GRAPPA reconstructions. *Magnetic Resonance in Medicine*. 2009; 62(3):739-746.
- (6) Arefeen Y, Beker O, Cho J, Yu H, Adalsteinsson E, Bilgic B. Scan-specific artifact reduction in k-space (SPARK) neural networks synergize with physics-based

reconstruction to accelerate MRI. *Magnetic Resonance in Medicine*. 2022;87(2):764-780.

- (7) Wang X, Ludwig D, Rawson M, Balan R, Ernst T. Estimating Noise Propagation of Neural Network Based Image Reconstruction Using Automated Differentiation. *Proceedings of the int. Soc. Magn Reson Med*. 2022, London. Abstract Number 0500.
- (8) Knoll F, Hammernik K, Zhang C, et al. Deep-learning methods for parallel magnetic resonance imaging reconstruction: a survey of the current approaches, trends, and issues. *IEEE Signal Processing Magazine*. 2020;37:128-140.
- (9) Cole E, Cheng J, Pauly J, Vasanawala S. Analysis of deep complex-valued convolutional neural networks for MRI reconstruction and phase-focused applications. *Magnetic Resonance in Medicine*. 2021;86(2):1093–1109.
- (10) Trabelsi C, Bilaniuk O, Zhang Y, Serdyuk D, Subramanian S, Santos JF, et al. Deep Complex Networks. In *Proceedings of the 6th International Conference on Learning Representations, (ICLR 2018), Conference Track Proceedings, Vancouver, British Columbia, Canada, 2018*.
- (11) Brau AC, Beatty PJ, Skare S, Bammer R. Comparison of reconstruction accuracy and efficiency among autocalibrating data-driven parallel imaging methods. *Magnetic Resonance in Medicine* 2008;59(2):382-395.
- (12) Kingma DP, Ba J. Adam: A Method for Stochastic Optimization. In *Proceedings of 3rd International Conference on Learning Representations, ICLR San Diego, CA, USA, 2015*.
- (13) Wang Z, Bovik AC, Sheikh HR, Simoncelli EP. Image quality assessment: from error visibility to structural similarity. *IEEE Trans Image Process*. 2004;13(4):600–612.
- (14) Uecker M, Lai P, Murphy MJ, Virtue P, Elad M, et al. ESPIRiT—an eigenvalue approach to autocalibrating parallel MRI: Where SENSE meets GRAPPA. *Magnetic Resonance in Medicine*. 2014;71(3):990-1001.
- (15) Paszke A, Gross S, Massa F, Lerer A, Bradbury J, Chanan G, et al. PyTorch: An Imperative Style, High-Performance Deep Learning Library. In *Proceedings of the 33rd Conference on Neural Information Processing Systems, Vancouver, Canada, 2019*.
- (16) Robson P, Grant A, Madhuranthakam A, Lattanzi R, Sodickson D, McKenzie C. Comprehensive quantification of signal-to-noise ratio and g-factor for image-based

and k-space-based parallel imaging reconstructions. *Magnetic Resonance in Medicine* 2008;60(4):895-907.

- (17) Baydin, Atilim Gunes; Pearlmutter, Barak; Radul, Alexey Andreyevich; Siskind, Jeffrey. Automatic differentiation in machine learning: a survey. *Journal of Machine Learning Research*. 2018;18: 1–43.
- (18) Massey, F. J., Jr. The Kolmogorov-Smirnov test for goodness of fit. *Journal of the American Statistical Association*. 1951;46:68–78.
- (19) Ding Y, Xue H, Ahmad R, Chang T, Ting ST, Simonetti OP. Paradoxical Effect of the Signal-to-Noise Ratio of GRAPPA Calibration Lines: A Quantitative Study. *Magnetic Resonance in Medicine*. 2015;74(1): 231-239.
- (20) Guo CG, Zhang L. A Novel Multiresolution Spatiotemporal Saliency Detection Model and Its Applications in Image and Video Compression. *IEEE Transactions on Image Processing*. 2010;19 (1):185–198.
- (21) Tong Y, Konik H, Cheikh F; Tremeau A. Full Reference Image Quality Assessment Based on Saliency Map Analysis. *Journal of Imaging Science and Technology*. 2010;54 (3): 30503–1–30503-14
- (22) Arun N, Gaw N, Singh P, Chang K, Aggarwal M, Chen B, Hoebel K, et al. Assessing the Trustworthiness of Saliency Maps for Localizing Abnormalities in Medical Imaging. *Radiology: Artificial Intelligence*. 2021;3(6)
- (23) Ayhan MS, Kümmerle LB, Kühlewein L, Inhoffen W, Aliyeva G, Ziemssen F, Berens P. Clinical validation of saliency maps for understanding deep neural networks in ophthalmology. *Medical Image Analysis*. 2022;77(102364).
- (24) Wang K, Angelopoulos A, De Goyeneche A, Kohli A, Shimron E, Yu S, Malik J, Lustig M. Rigorous Uncertainty Estimation for MRI Reconstruction. *Proceedings of the ISMRM 2022, London*. Abstract #0749.
- (25) Fischer, P., Thomas, K., Baumgartner, C.F. (2023). Uncertainty Estimation and Propagation in Accelerated MRI Reconstruction. In: Sudre, C.H., Baumgartner, C.F., Dalca, A., Mehta, R., Qin, C., Wells, W.M. (eds) *Uncertainty for Safe Utilization of Machine Learning in Medical Imaging*. UNSURE 2023. *Lecture Notes in Computer Science*, vol 14291. Springer, Cham.

- (26) Edupuganti V, Mardani M, Vasanawala S, Pauly J. Uncertainty Quantification in Deep MRI Reconstruction. *IEEE Trans Med Imaging*. 2021 Jan;40(1):239-250.
- (27) Luo G, Blumenthal M, Heide M, Uecker M. Bayesian MRI reconstruction with joint uncertainty estimation using diffusion models. *Magn Reson Med*. 2023; 90: 295-311.
- (28) Breuer FA, Blaimer M, Mueller MF, Seiberlich N, Heidemann RM, Griswold MA, et al. Controlled aliasing in volumetric parallel imaging (2D CAIPINHA). *Magnetic Resonance in Medicine*. 2006;55(3):549–556.
- (29) Bilgic B, Gagoski BA, Cauley SF, Fan CA, Polimeni JR, et al. Wave-CAIPI for highly accelerated 3D imaging. *Magnetic Resonance in Medicine*. 2015;73(6):2152-2162.

Figures

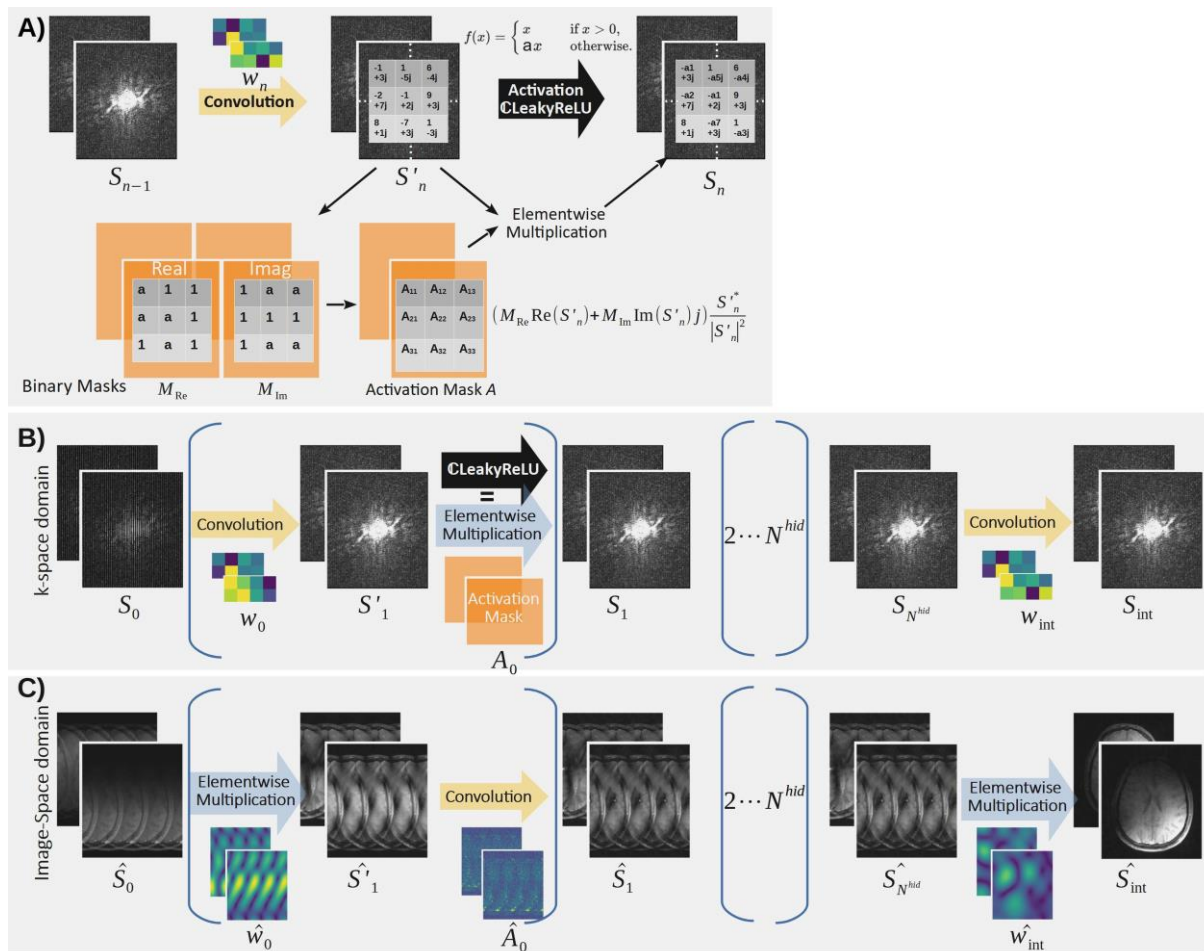


Figure 1: **(A)** The proposed formalism to express nonlinear activations in k-space as elementwise multiplication of the signal to be activated with an introduced activation mask A , which is obtained from binary masks M . The latter assign each k-space signal either the value 1 or a (i.e. the slope parameter of the CReLU activation function), depending on the sign of the signal. **(B)** The conventional RAKI reconstruction in the k-space, in which the training is performed. **(C)** RAKI inference in the image space (proposed method). According to the convolution theorem, convolutions in k-space are transferred into elementwise multiplications in image space, and elementwise multiplications in k-space are transferred into convolutions in image space. All operations are complex-valued.

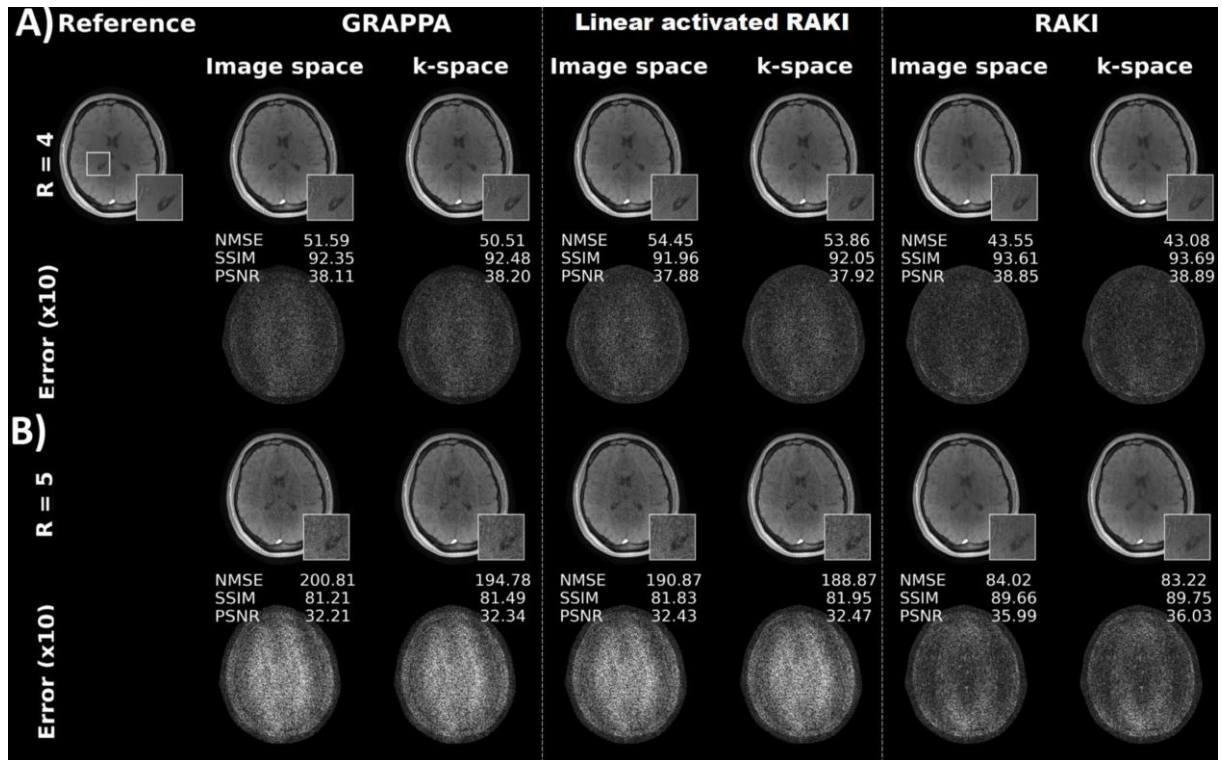


Figure 2: **(A)** GRAPPA, linear activated RAKI and RAKI reconstructions in the k-space and in the image space of the FLASH dataset at 4-fold **(B)** and at 5-fold retrospective undersampling. The reconstruction weights are trained in the k-space, but the inferences in image space are quasi-identical to inferences in k-space. The RAKI reconstructions with linear activations converge towards GRAPPA, exhibiting similar noise enhancement and quantitative metrics. However, RAKI with nonlinear activations shows strong noise resilience, pronouncing the importance of nonlinear activations. The error maps are shown below and scaled for display. Quantitative metrics include the normalized mean squared error (NMSE), structural similarity index measure (SSIM), peak signal to noise ratio (PSNR).

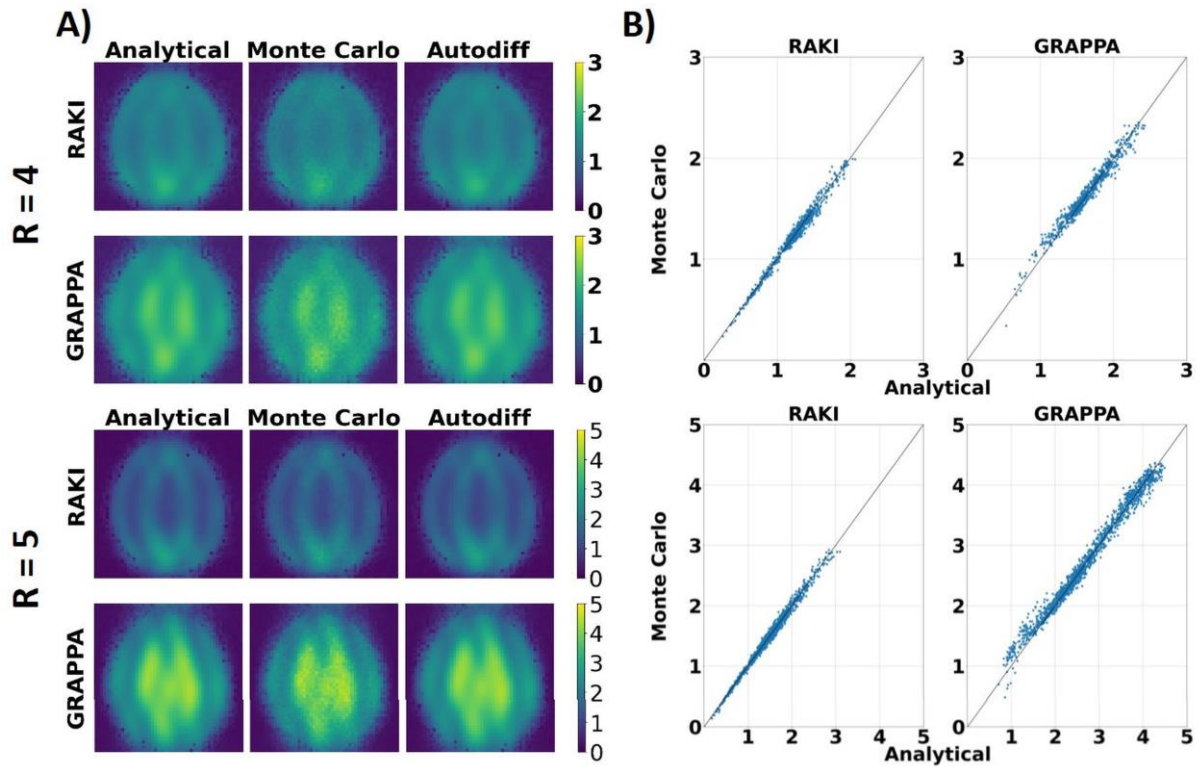


Figure 3: **(A)** G-factor maps (50x50 low resolution images) computed via analytical expression, via Monte-Carlo simulations, and via auto-differentiation for image reconstructions for 4-fold retrospective undersampling ($R=4$, top), and for 5-fold undersampling ($R=5$, bottom). The corresponding images are displayed in Figure 2. **(B)** Analytically obtained g-factors of all voxels are plotted against the g-factors obtained via the Monte-Carlo simulations. A good agreement is demonstrated for both 4- and 5-fold undersampling.

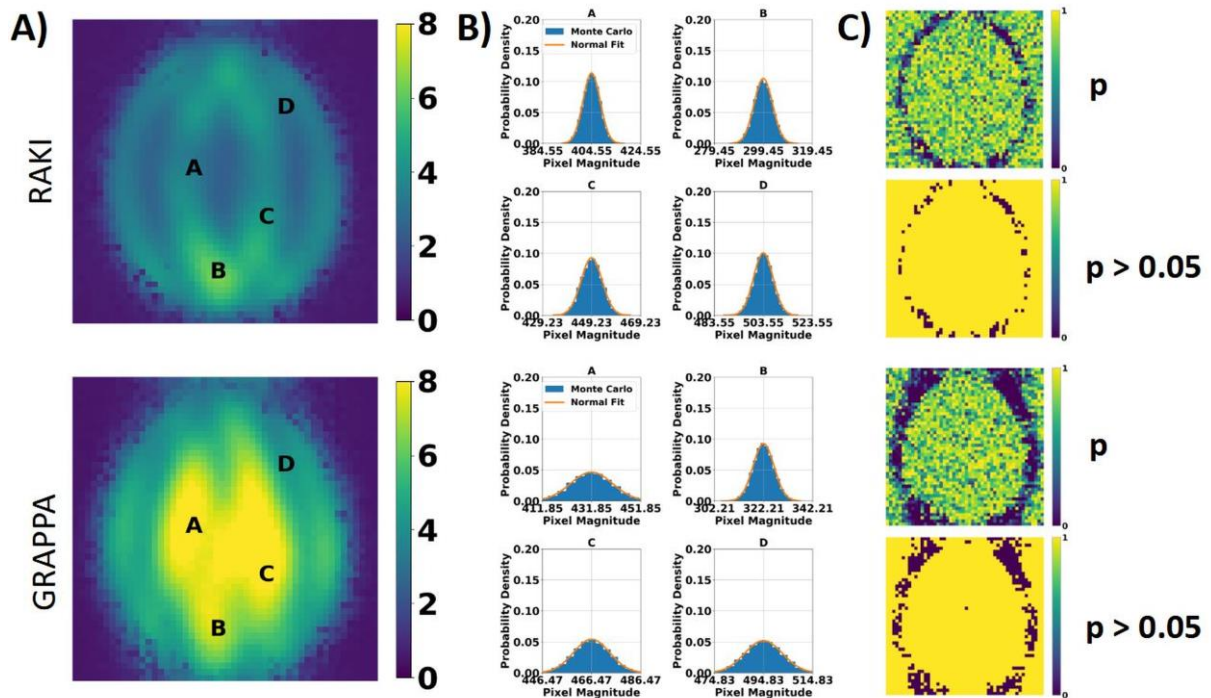


Figure 4: **(A)** Standard deviation maps obtained from Monte-Carlo simulations for RAKI and GRAPPA reconstructions of 5-fold undersampled FLASH dataset. **(B)** Voxel magnitude histograms of 10,000 pseudo replicas obtained from voxel locations indexed by A-D in **(A)**, and corresponding fitted normal distributions. **(C)** P-value maps computed in Kolmogorov-Smirnov tests for normality, and binary masks where $p > 0.05$, which is the significance level not to reject the null hypothesis (i.e. voxel magnitude distributions of pseudo replicas are normal). For almost all voxels in the region of interest, a normal distribution can be assumed for both RAKI and GRAPPA, which validates the use of the generalized g-factor computation for RAKI.

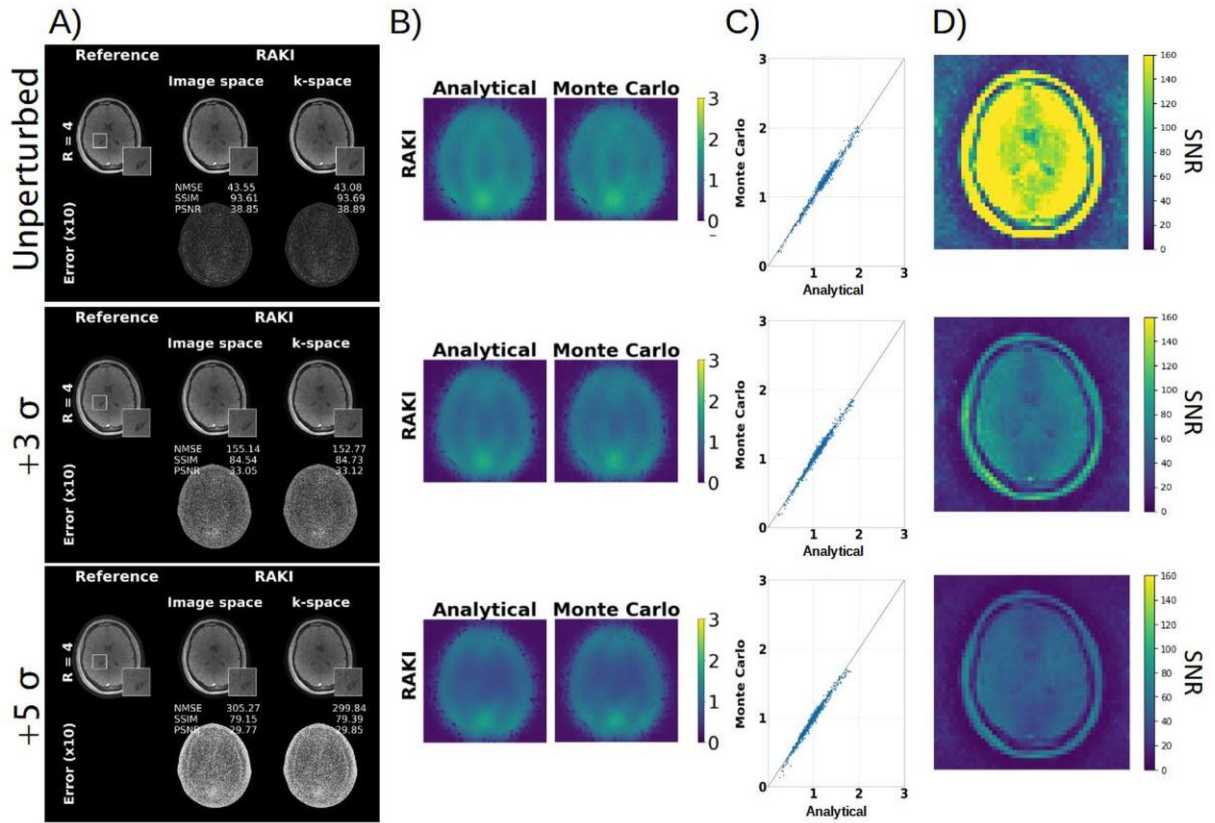


Figure 5: **(A)** RAKI image reconstructions and error maps for 4-fold undersampled FLASH dataset (without additive noise superimposition, i.e. unperturbed, and with random Gaussian noise superimposition with standard deviation of 3σ and 5σ and zero mean). **(B)** RAKI g-factor maps obtained analytically and via Monte-Carlo simulations. **(C)** G-factors of all voxels computed analytically plotted against g-factors obtained via the Monte-Carlo simulations shown in (B). **(D)** SNR maps of images in (A) obtained via the Monte-Carlo simulations.

Supporting Material

Figure S1

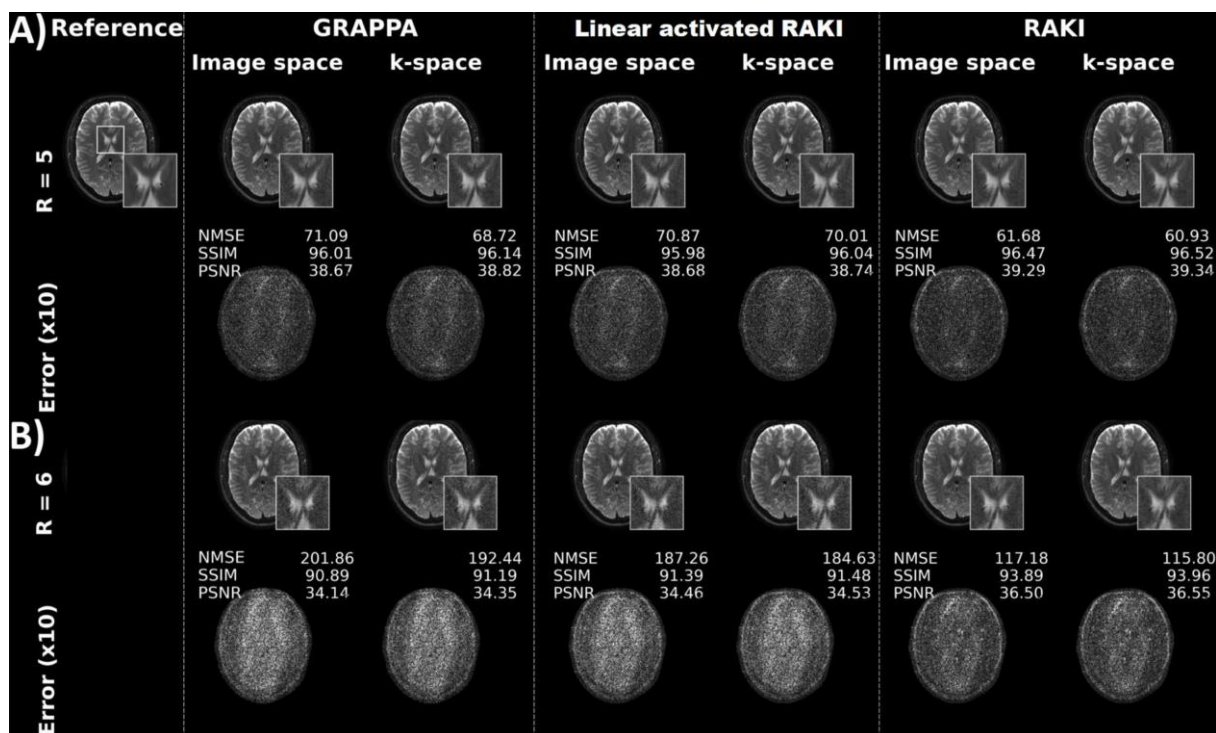


Figure S1: **(A)** GRAPPA, linear activated RAKI and RAKI reconstructions in the k-space and in the image space of the TSE dataset at 5-fold **(B)** and at 6-fold retrospective undersampling. The reconstruction weights are trained in the k-space, but the inferences in image space are quasi-identical to inferences in k-space. The RAKI reconstructions with linear activations converge towards GRAPPA, exhibiting similar noise enhancement and quantitative metrics. However, RAKI with nonlinear activations shows strong noise resilience, pronouncing the importance of nonlinear activations. The error maps are shown below and scaled for display. Quantitative metrics include the normalized mean squared error (NMSE), structural similarity index measure (SSIM), peak signal to noise ratio (PSNR).

Figure S2

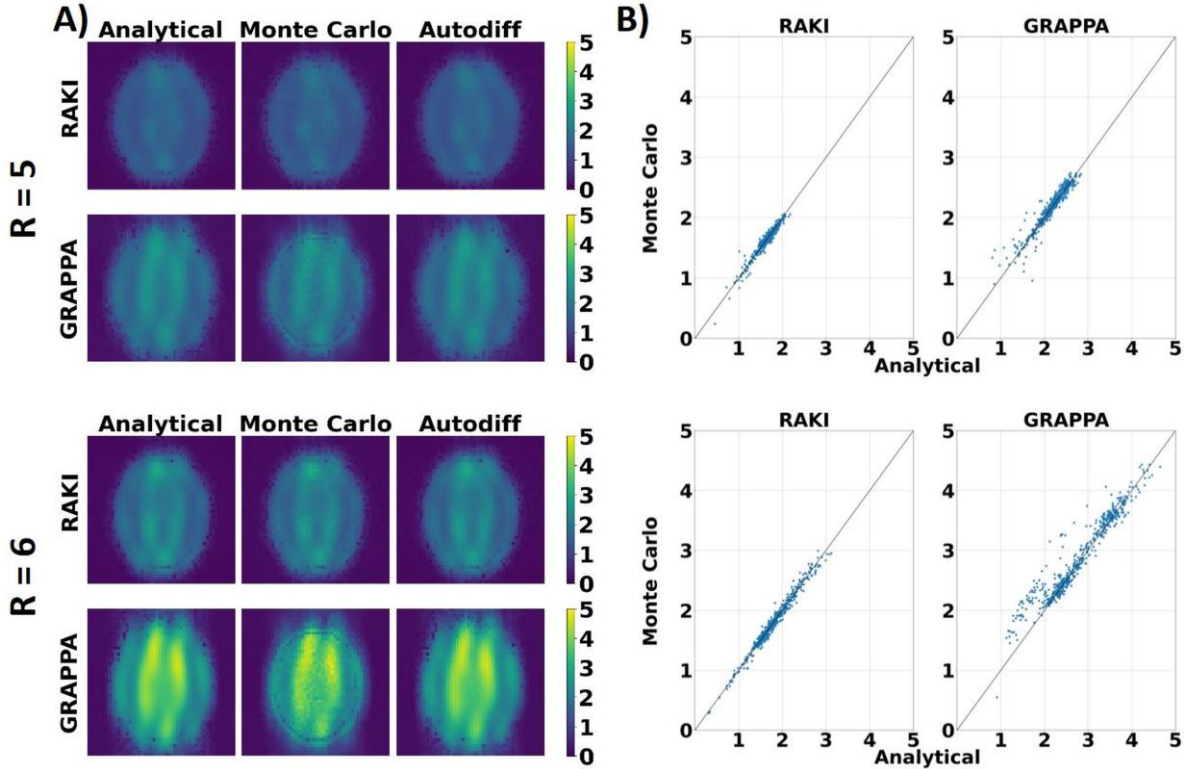


Figure S2: **(A)** G-factor maps (50x50 low resolution images) computed via analytical expression, via Monte-Carlo simulations, and via auto-differentiation for image reconstructions for 5-fold retrospective undersampling ($R=5$, top), and for 6-fold undersampling ($R=6$, bottom). The corresponding images are displayed in Figure S1. **(B)** Analytically obtained g-factors of all voxels are plotted against the g-factors obtained via the Monte-Carlo simulations. A good agreement is demonstrated for both 5- and 6-fold undersampling.

Figure S3

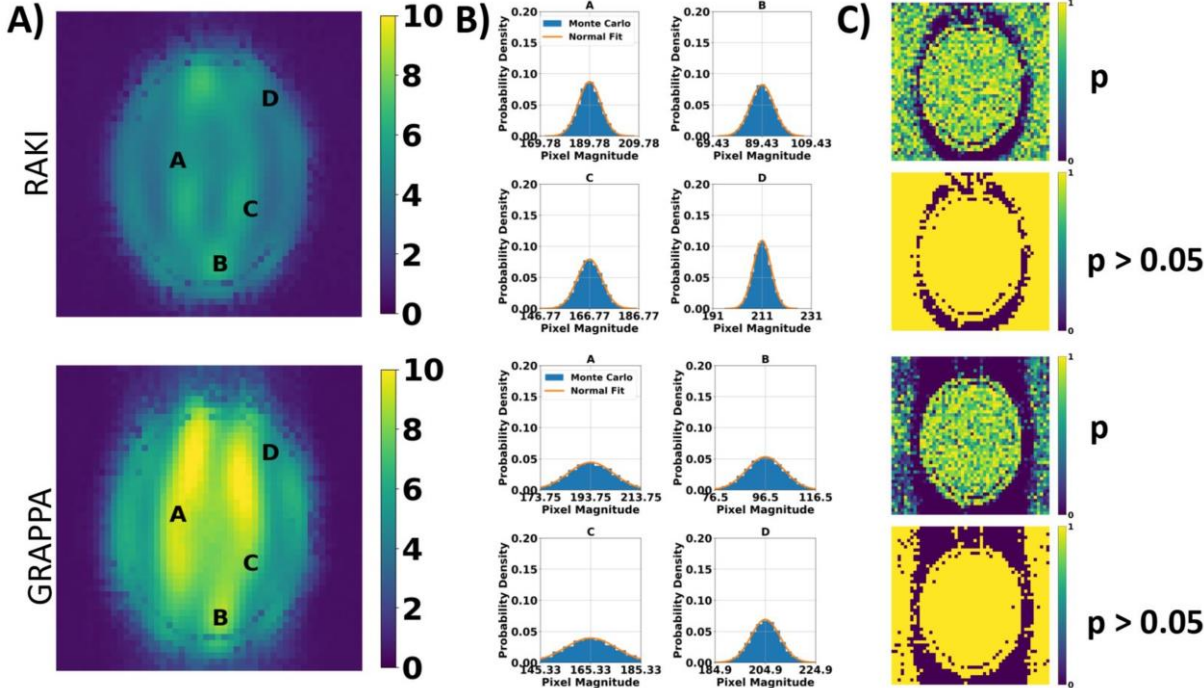


Figure S3: **(A)** Standard deviation maps obtained from Monte-Carlo simulations for RAKI and GRAPPA reconstructions of 6-fold undersampled TSE dataset. **(B)** Voxel magnitude histograms of 10,000 pseudo replicas obtained from voxel locations indexed by A-D in **(A)**, and corresponding fitted normal distributions. **(C)** P-value maps computed in Kolmogorov-Smirnov tests for normality, and binary masks where $p > 0.05$, which is the significance level not to reject the null hypothesis (i.e. voxel magnitude distributions of pseudo replicas are normal). For almost all voxels in the region of interest, a normal distribution can be assumed for both RAKI and GRAPPA, which validates the use of the generalized g-factor computation for RAKI.

Figure S4

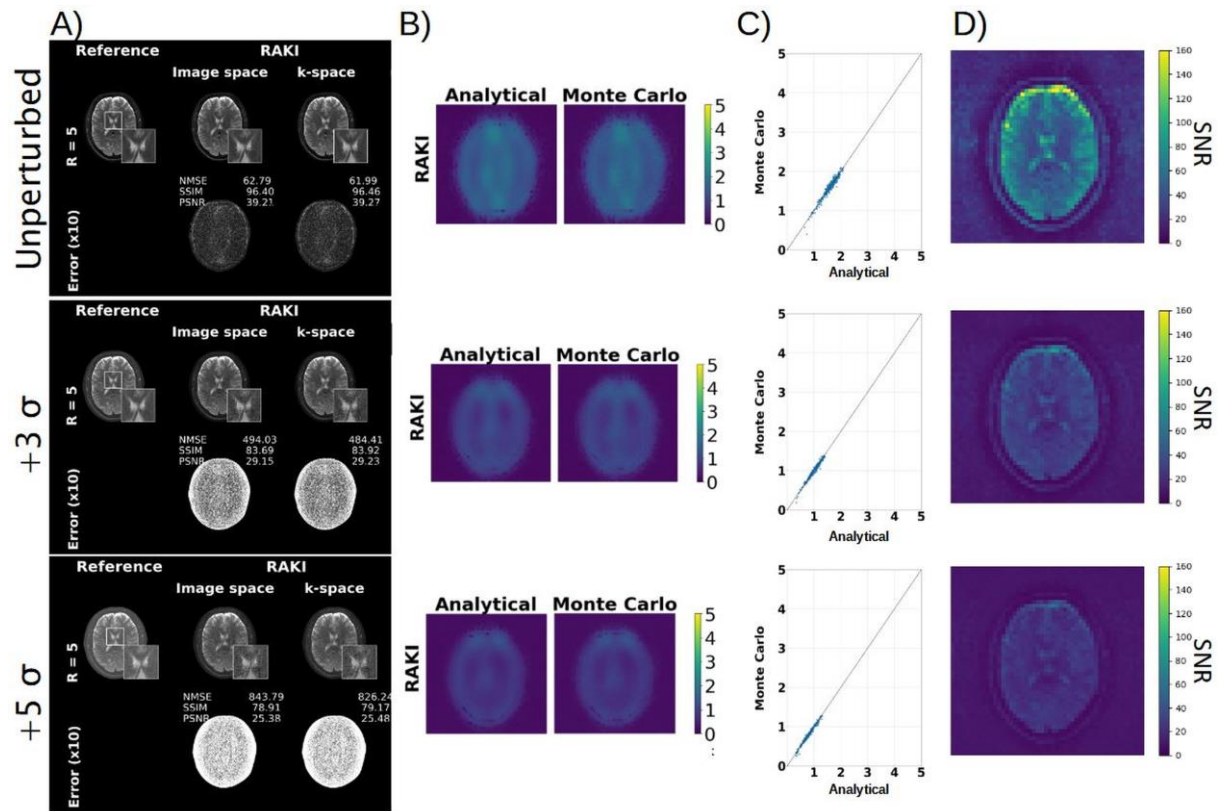


Figure S4: **(A)** RAKI image reconstructions and error maps for 5-fold undersampled TSE dataset (without additive noise superimposition, i.e. unperturbed, and with random Gaussian noise superimposition with standard deviation of 3σ and 5σ and zero mean. **(B)** RAKI g-factor maps obtained analytically and via Monte-Carlo simulations. **(C)** G-factors of all voxels computed analytically plotted against g-factors obtained via the Monte-Carlo simulations shown in (B). **(D)** SNR maps of images in (A) obtained via the Monte-Carlo simulations.